Inner Structure of Atmospheric Inversion Layers over Haifa Bay in the Eastern Mediterranean

N. Haikin, E. Galanti, T. G. Reisin, Y. Mahrer & P. Alpert

Boundary-Layer Meteorology
An International Journal of Physical, Chemical and Biological Processes in the Atmospheric Boundary Layer

ISSN 0006-8314
Volume 156
Number 3

Boundary-Layer Meteorol (2015)
156:471-487
DOI 10.1007/s10546-015-0038-4

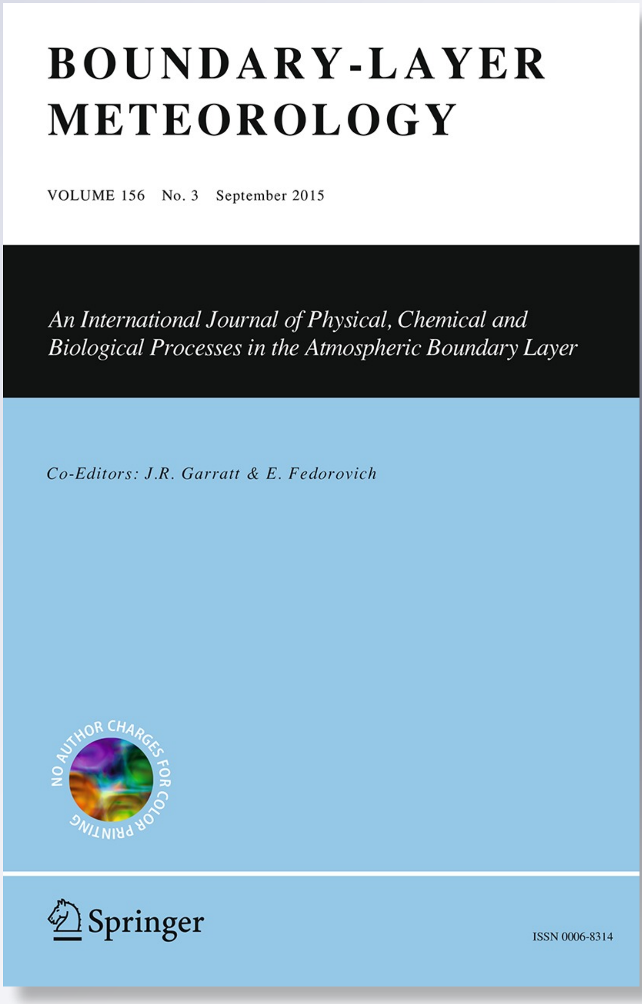

Springer

Boundary-Layer Meteorol (2015) 156:471–487
DOI 10.1007/s10546-015-0038-4

ARTICLE

Inner Structure of Atmospheric Inversion Layers over Haifa Bay in the Eastern Mediterranean

N. Haikin[1,2] · E. Galanti[3] · T. G. Reisin[4] · Y. Mahrer[5] · P. Alpert[1]

Received: 18 June 2014 / Accepted: 28 April 2015 / Published online: 24 May 2015

Abstract Capping inversions act as barriers to the vertical diffusion of pollutants, occasionally leading to significant low-level air pollution episodes in the lower troposphere. Here, we conducted two summer campaigns where global positioning system radiosondes were operated in Haifa Bay on the eastern Mediterranean coast, a region of steep terrain with significant pollution. The campaigns provided unique high resolution measurements related to capping inversions. It was found that the classical definition of a capping inversion was insufficient for an explicit identification of a layer; hence additional criteria are required for a complete spatial analysis of inversion evolution. Based on the vertical temperature derivative, an inner fine structure of inversion layers was explored, and was then used to track inversion layers spatially and to investigate their evolution. The exploration of the inner structure of inversion layers revealed five major patterns: symmetric peak, asymmetric peak, double peak, flat peak, and the zig-zag pattern. We found that the symmetric peak is related to the strongest inversions, double peak inversions tended to break apart into two layers, and the zig-zag pattern was related to the weakest inversions. Employing this classification is suggested for assistance in following the evolution of inversion layers.

Keywords Capping inversion · Inner structure · Inversion · Radiosonde

✉ N. Haikin
nitsahai@post.tau.ac.il

1 Department of Geophysics, Atmospheric and Planetary Sciences, Tel-Aviv University, 69978 Ramat-Aviv, Tel Aviv, Israel

2 NRC Negev, POB 9001, 84190 Beer Sheva, Israel

3 Department of Earth and Planetary Sciences, Weizmann Institute of Science, Rehovot, Israel

4 Soreq NRC, 81800 Yavne, Israel

5 Soil and Water Department, Faculty of Agriculture, Hebrew University, Rehovot, Israel

1 Introduction

The atmospheric boundary layer (ABL) has been long studied, with an emphasis on its daily and periodically varying depth (e.g., Deardorff 1979; Stull 1991; Berner et al. 2011). The depth of the ABL is a dynamic parameter, influenced by synoptic conditions and by local conditions such as topography-induced wind and temperature, land cover as well as land use. The definition of the ABL top, or the mixing height, requires suitable data or parametrization, which are frequently missing or insufficient, especially for operational purposes such as air pollution control. The ABL depth can be derived using several definitions, based on measurements or on calculations: the size of the entrainment zone, the average depth of the mixing layer or the mid-height of the entrainment zone—z_i, the Richardson number (Ri), the height at which fluxes decay or by the observed elevation of a stable layer. However, each of the above parameters might contain large uncertainties (Seibert et al. 2000). This issue was studied extensively by others, under various inversion strengths, wind and stability state, and different buoyancy conditions. The entrainment zone is the region between the highest level reached by thermals and the lowest level attained by free atmospheric air (Deardorff et al. 1980), or a zone that is not well-mixed and where turbulence intensity declines towards its top. Characterization and parametrization schemes of the entrainment zone depth and elevation for the purpose of prediction were attempted in many studies (e.g., Tennekes 1973; Zeman and Tennekes 1977; Mahrt 1979; Deardorff et al. 1980; Gryning and Batchvarova 1994; Sullivan et al. 1998; Berner et al. 2011). Melas et al. (1995) suggested that the thickness of the coastal entrainment zone is 20–30 % of the mixed-layer depth except for the zone close to the shoreline where the entrainment zone thickness is comparable with the depth of the mixing layer. The mixed-layer height z_i is usually defined as the level at which the heat flux changes its sign (Seibert et al. 2000).

The stable layer at the ABL top is occasionally referred to as "the inversion", independent of its lapse rate (Stull 1988), or "the capping inversion" (Piringer et al. 1998; Fedorovich and Mironov 1995; Jones et al. 2011). Sun (2009) suggested the inversion thickness was between $0.1z_i$ to $0.3z_i$. Gossard et al. (1985) used data from a 300 m tower, acoustic and radar sounders and radiosonde, to study the fine structure of stable layers in atmospheric profiles. They found elevated superadiabatic zones in atmospheric profiles with large upward heat fluxes, which included elevated stable layers. Lidar studies have been used to correlate the entrainment rate and the entrainment-zone thickness with the stability at the top of the convective boundary layer (CBL), where the stability is quantified by using a Richardson number (Ri) (Kiemle et al. 1997; Brooks 2003; Grabon et al. 2010). Martucci et al. (2007) used backscatter lidar to retrieve the mixed-layer depth and the residual-layer height, which were well correlated with the capping inversions retrieved from radiosonde data. Sullivan et al. (1998) used large-eddy simulations to study the spatial-temporal evolution of the capping inversion, with respect to the entrainment rate and to the inversion elevation, strength and thickness dimensions. Rampanelli and Zardi (2004) suggested an algorithm for calculating the capping inversion above the CBL, regarding its height and strength. Metcalf (1975) investigated gravity waves within a strong inversion layer, and Saiki et al. (2000) observed a capping inversion with temperature fluctuations that corresponded to the presence of gravity waves.

A comprehensive characterization of the capping inversion and its dynamics would be most valuable for ABL thermodynamic and air pollution studies. While former studies assumed a simple inner structure, and focused on the spatial-temporal variations of the capping inversion elevation, here the focus is on the inner structure of the capping inversion and other elevated inversions. An emphasis is placed on the identification and analysis of inversion-

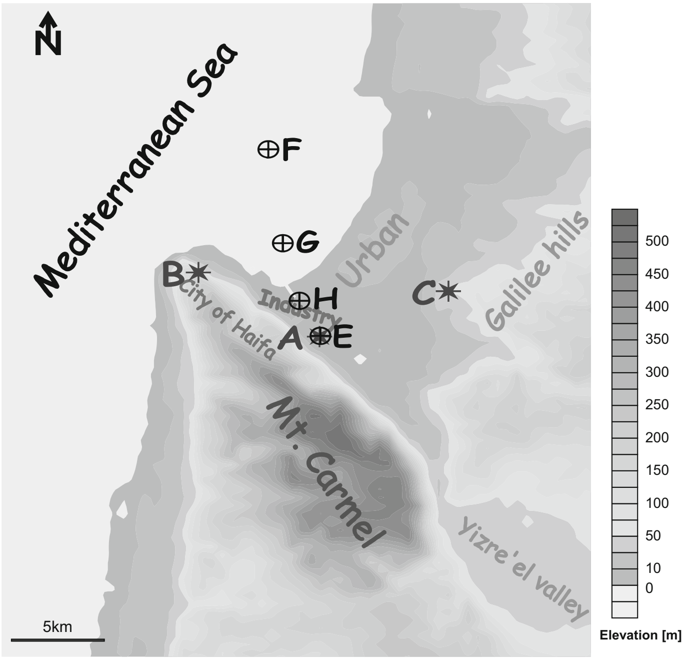

Fig. 1 Map of the Haifa region: the Mediterranean Sea on the west, Mt. Carmel rises from the coastline with the city of Haifa on its northern top and slopes, urbanized zone in the Haifa Bay north to Mt. Carmel, and the Galilee hills on the east. Radiosondes launching sites: *A*–*C* represent Aug08, *E*–*H* represent onshore and offshore sites of Aug09 (note: *A* and *E* represent the same location)

layer characteristics and structure, particularly those of the capping inversion. We propose a new approach for explicit identification of an inversion layer, based on its inner structure. Although we include data from a limited amount of atmospheric profiles, the patterns suggested here were identified in all profiles. Data from an independent campaign (different season) support the present results.

In Sect. 2 the methodology of this study is presented while in Sect. 3 the identified inner structure of the inversion layer is discussed, first defined for the capping inversions. In Sect. 3.2 categories of the identified structures are presented, and in Sect. 3.3 three cases of inversion evolution are discussed, based on their identified inner structures.

2 Methodology

Summertime in the Mediterranean region is dominated by synoptic-scale anticyclones and large-scale subsidence (Alpert et al. 1990; Kallos et al. 2007). The coastal daily circulation, with humid air advected from the sea and hot dry air from above, results in the formation of a semi-permanent marine inversion over Israel. This inversion, however, varies in depth and height. The Shallow Persian Trough synoptic pressure system is characterized by a shallow mixed layer capped by subsiding warm and dry air and thus reduces ventilation within the inversion-capped mixed layer. Air pollution studies of this region have identified this synoptic category as being the main one affecting pollutant dispersion, especially in the coastal zone (Dayan and Koch 1988; Koch and Dayan 1992).

Table 1 Location and time of the 19 radiosonde launches in this study

	Date	Site	Time (LT)	Synoptic system
1	4 August 2008	C	1715	Persian Trough with small cyclone over Cyprus. Deeper trough on 5 August
2		B	1900	
3	5 August 2008	A	0510	
4		B	0615	
5		A	0720	
6		C	1400	
7		C	1645	
8		B	1830	
9	6 August 2008	A	0450	
10		B	0610	
11		A	0735	
12		A	1330	
13	24 August 2009	F	1800	Persian Trough with small cyclone over Cyprus. Deeper trough on 25 August
14		H	2000	
15		E	0130	
16		H	0605	
17	25 August 2009	G	1235	
18		H	1420	
19		E	1550	

Two summer upper-air campaigns were conducted in August 2008 and August 2009 in the Haifa region on the eastern Mediterranean coast, from which 19 atmospheric profiles were retrieved. The prevailing synoptic system during both summer campaigns was a Persian Trough, which forces daily westerly to north-westerly winds in this region, while the sea breeze is mostly from the west or the north-west. The study domain has complex terrain, with Mt. Carmel rising from the coastline up to 450 m over a horizontal distance of about 10 km. The August 2008 campaign (hereby "Aug08") was planned for intensive measurements around sunrise and sunset, aiming to capture the rapid ABL and capping inversion evolution over these hours. Midday launches were included to measure the peak capping inversion level. The August 2009 campaign (hereby "Aug09") was aimed to obtain atmospheric profiles both offshore and onshore, including radiosonde launches in the transition hours, and at midday and midnight.

A GPS-based radiosounding system was used, with a sampling frequency of 1 Hz and a vertical resolution of about 5 m (depending on local vertical velocity fluctuations). The system is capable of providing very high resolution profiles of wind speed and direction (based on differential positioning), temperature (thermistor-based sensor), pressure and relative humidity. Wind-speed and temperature profiles were measured to an absolute accuracy of $0.15\,\mathrm{m\,s^{-1}}$ and 0.5 °C, and resolution of $0.01\,\mathrm{m\,s^{-1}}$ and 0.1 °C, respectively.

The inversion layers in all thermal profiles were identified as follows: the inversion base elevation was defined as the first level with $\mathrm{d}T/\mathrm{d}Z > 0$, where Z denotes the elevation above mean sea level and T is air temperature, followed by a continuous positive (first-order forward) derivative for at least 50 m which corresponds to a minimum of ten successive data points. In Fig. 1 the radiosonde locations are shown, with A–C representing the Aug08 sites and E–H the Aug09 sites. Note that A and E refer to the same site. Table 1 presents the

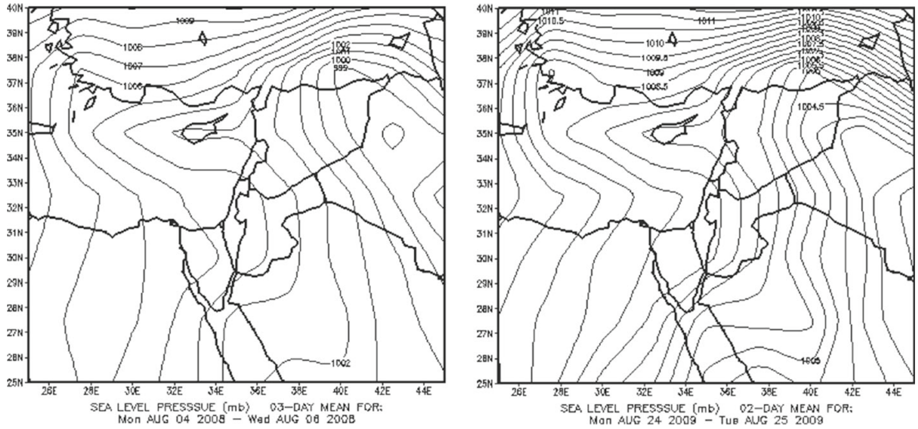

Fig. 2 Synoptic maps: 4–6 August 2008 (*left*), 24–25 August 2009 (*right*). Both campaigns were under Persian Trough conditions. Maps are from NCEP operational data site, at: http://www.esrl.noaa.gov/psd/cgi-bin/data/histdata

time and location of the 19 launches, while Fig. 2 presents sea-level pressure analyses of the campaign days (maps were created from the NCEP operational data).

3 Results

3.1 General Features

The observed capping-inversion-base heights (H_b) were found to be similar to the CBL mean depth as reported by Koch and Dayan (1992). The average capping-inversion thickness (ΔH) was about 130 m, similar to the range of 100–200 m as reported in Grabon et al. (2010) who used lidar to determine the transition zone at the ABL top. The current study is based on local soundings and therefore refers to local inversion layers and at a specific time rather than to average values. Here, the analysis of the inversion layers showed that, even high resolution information of ΔH was insufficient to define an inversion layer (Sect. 3.2). Figure 3 shows the measured capping-inversion-base height (H_b) as observed for both campaigns under similar prevailing synoptic conditions. The diurnal cycle is clearly present, with the smallest H_b before sunrise and the largest in the afternoon. Although H_b is expected to decrease significantly only after or close to sunset when turbulence decays (Stull 1988), the observations show a significant decrease throughout the afternoon. This may be due to the strong sea-breeze circulation for this period in this region, which weakens the vertical circulation as illustrated by Uzan and Alpert (2012) employing profiler data on the coast south of Haifa.

For the analysis of H_b and ΔH observations were classified into daytime and nighttime, where "nighttime" was defined as the time after sunset and before sunrise. Two evening observations were also included in the night group (1830 LT and 1900 LT (site B) in Fig. 3). Figure 4 shows the two data groups, where it can be seen that the range of ΔH of the daytime values is about half the range of nighttime ones, while H_b values present approximately a 300 m range of each group (between the dashed lines). Three data points, of which one "night" value was in the "day" zone and two "day" values were in the "night" zone of H_b (*circled*), are discussed in Sect. 3.2.

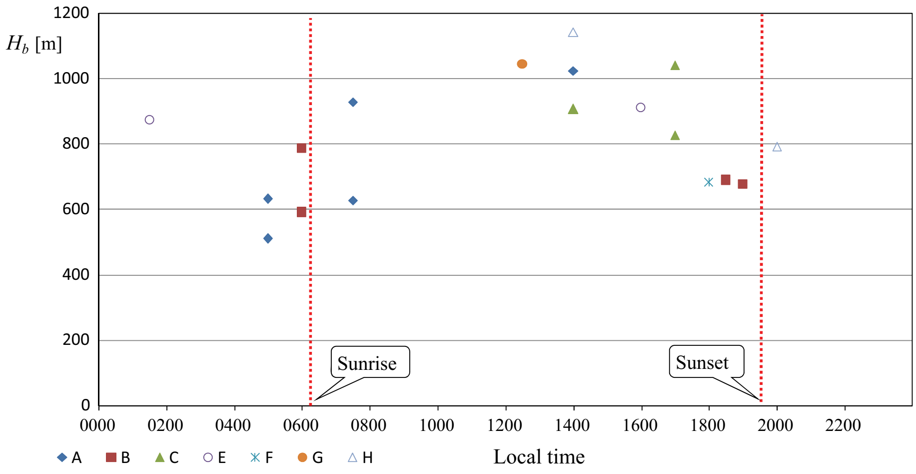

Fig. 3 Capping-inversion-base height (H_b) from 18 atmospheric profiles observed over Haifa Bay for Aug08 and Aug09 campaigns, presented on a 24-h time scale (LT). Sunrise and sunset times are marked with *vertical lines*. The *legends* denote the site (Fig. 1) of launching

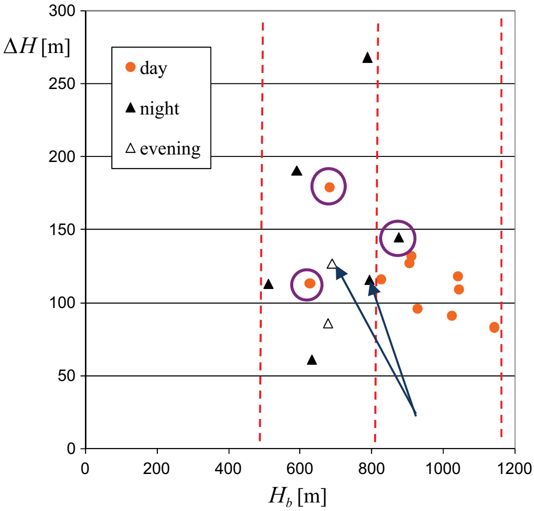

Fig. 4 Capping-inversion thickness ΔH [m] (z axis) versus inversion-base elevation H_b [m]. Data points are classified as: "night" (after sunset and before sunrise, *triangles*), "day" (*circles*), "evening" (*white triangles*). *Vertical dashed lines* separate between "night' and "day" groups. A couple of adjacent points marked with *arrows*, are discussed in Sect. 3.2.2. Three exceptional points are *circled*: two "day" points in the "night" zone and one "night" point in the "day" zone, these points are discussed in Sect. 3.2.3

3.2 Explicit Identification of Inversion Layers

The difficulty of tracking variations in inversion layers between launches, particularly the changes in the capping inversion, raised some fundamental questions:

- Why consecutive profiles did not have the same number of inversion layers?
- Which inversions vanished or merged into other inversion layers?
- How is it possible to ensure that the same particular layer is being tracked?

Evidently, a more precise identification of an inversion layer is required. In the following section we present and discuss the inner structures of the inversion layers which were identified based on the thermal stratification within the layers.

Fig. 5 An example of a sub-layer structure of an inversion layer. The x-axis denotes the temperature lapse rate $\mathrm{d}T/\mathrm{d}Z$ [K $(100\ \mathrm{m})^{-1}$] and z-axis denotes the relative height in the layer [m]. This layer was extracted from a profile observed over site C 5 August 2008 at 1400 LT

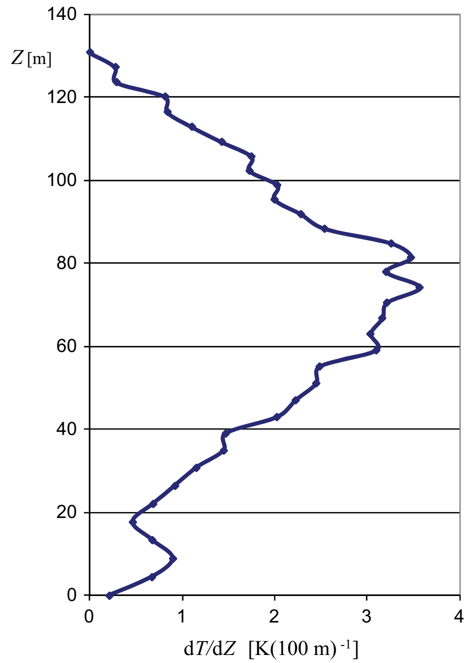

3.2.1 Basic Structure

In most studies, three parameters are used to identify a specific inversion layer: H_b—the elevation of the inversion base, the level where $\mathrm{d}T/\mathrm{d}Z$ becomes positive; ΔH—thickness of the inversion layer, i.e. the total depth in which $\mathrm{d}T/\mathrm{d}Z$ remains positive; $\Delta T_{\mathrm{layer}}$—the temperature change across the whole inversion layer. These parameters, however, are not sufficient for an explicit identification of a specific layer. Analysis of the sub-layer thermal profile within the inversion layers revealed a more complex structure. An example of a sub-layer structure of an inversion layer in the profile attained over site C, 5 August 2008 at 1400 LT, is shown in Fig. 5. For convenience, the unit of K $(100\,\mathrm{m})^{-1}$ was used for $\mathrm{d}T/\mathrm{d}Z$ (x-axis), while the z-axis denotes the relative height in the inversion layer. The structure in Fig. 5 has a triangular shape with a $\mathrm{d}T/\mathrm{d}Z$ peak of about 3.5 K $(100\,\mathrm{m})^{-1}$ located close to half its height. Hence, this pattern was classified as a symmetric peak (see Sect. 3.3).

3.2.2 A Comparison of Two Capping Inversions

Capping inversions that are represented by two adjacent points in Fig. 4 (marked with arrows) were analyzed and compared; their dimensions showed similar features (see Table 2). Sub-layer analysis revealed two primary peaks with gradient values of 5.8 and 4.9 K $(100\ \mathrm{m})^{-1}$, and smaller local peaks with similar coordinates (Fig. 6). The primary peak was defined as the maximum $\mathrm{d}T/\mathrm{d}Z$ [K $(100\ \mathrm{m})^{-1}$] in the inversion layer, while peak symmetry was defined as the peak location on a normalized z-axis, where the value 0.50 represents perfect symmetry. The peak symmetrical/asymmetrical characteristics were later used as a primary criterion for the inner structure classification (Sect. 3.3). The inner structures of these two

Table 2 Dimensions of the two inner structures presented in Fig. 6: the capping-inversion thickness ΔH [m]; the inversion-base height H_b [m]; primary peaks and their symmetry; the temperature change across the inversion layer ΔT_{layer} [°C]; calculated area of the structure $\Sigma_0^n(\Delta X_j \cdot \Delta Z_j)$

Time (LT)	1900	2000
Campaign	Aug08	Aug09
ΔH [m]	127	119
H_b [m]	690	790
Primary peak [K (100 m)$^{-1}$]	5.8	4.9
Peak symmetry	0.66	0.59
ΔT_{layer} [°C]	3.51	3.13
Area $\Sigma_0^n(\Delta X_j \cdot \Delta Z_j)$	2.764	2.702

The Aug08 inversion was observed over site B and the Aug09 inversion over site H

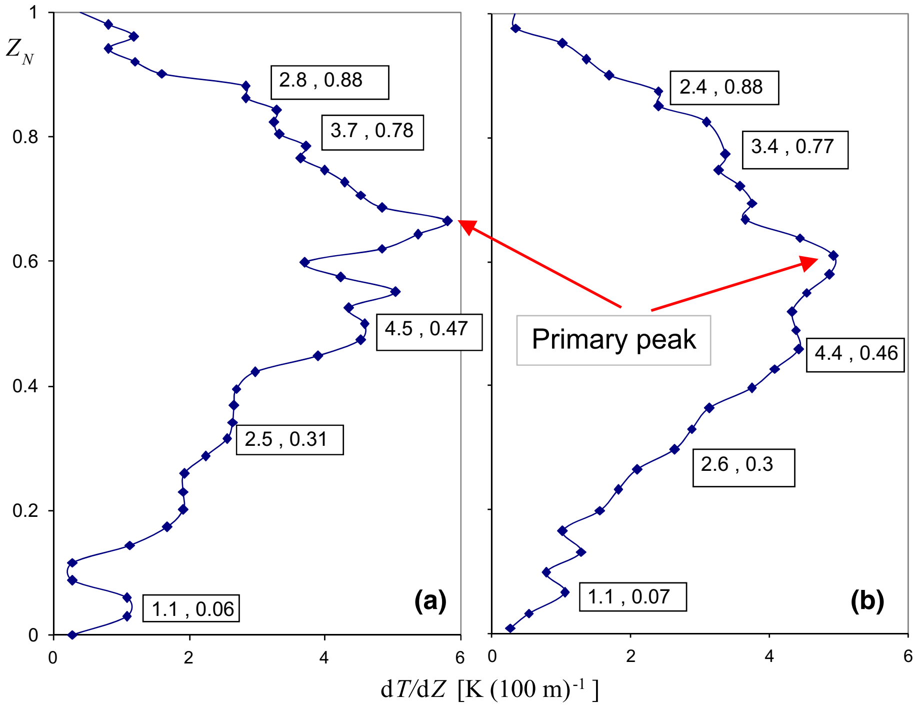

Fig. 6 The inner structure of two evening capping inversions derived from atmospheric profiles observed over site B (4 August 2008 at 1900 LT, panel **a**), and over site H (24 August 2009 at 2000 LT, panel **b**). The x-axis denotes dT/dZ [K (100 m)$^{-1}$], the z-axis denotes the normalized height Z_N [by 127 m (**a**) and by 119 m (**b**)]. Coordinates of corresponding local peaks are marked as (x, z)

capping inversions are presented in Fig. 6 with normalized Z_N, where coordinates (x, z) of the apparently corresponding local peaks are presented.

Interestingly, the two capping inversions were each observed in different campaigns, with a one-year difference between them, where the Aug08 inversion was observed over site B and Aug09 over site H. This finding suggests that the regional and seasonal (or synoptic

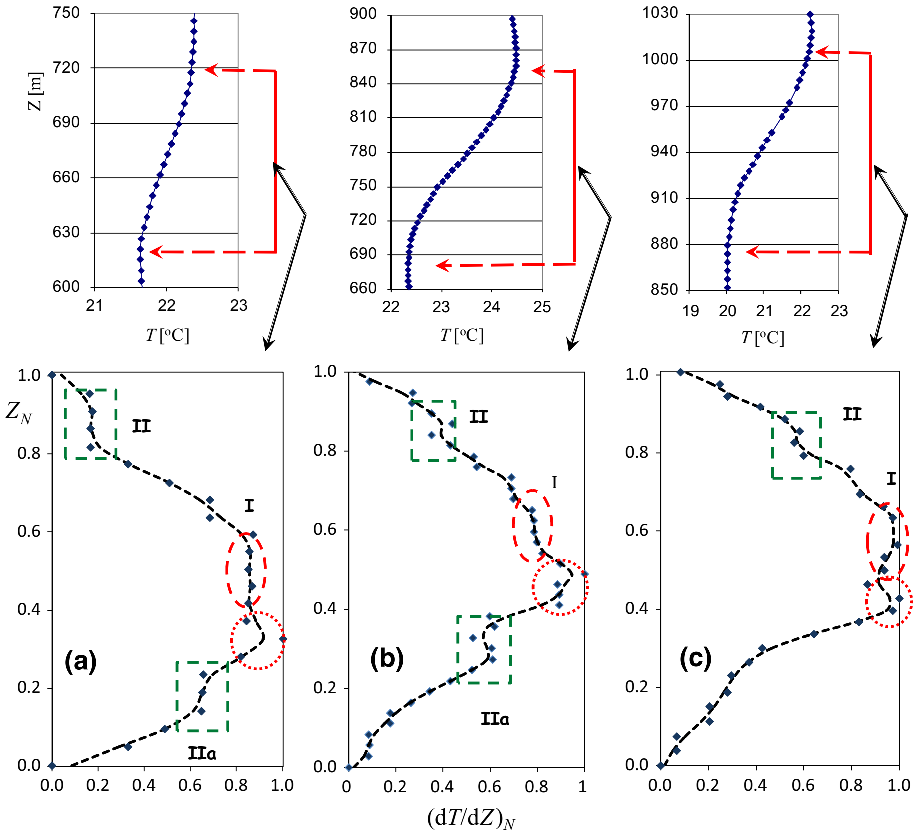

Fig. 7 The *upper panels* show the three capping inversions as observed (T [°C] vs. Z [m]), the *dashed arrows* point at the inversion edges. The *lower panels* present the inner structures with normalized Z_N and $(\mathrm{d}T/\mathrm{d}Z)_N$. The structures have primary peaks with narrow maximum and flat "shoulders" (*circles* & *ellipse* respectively, marked as I), and secondary peaks (*rectangles*, marked as II and IIa). Smoothed pattern is the *dashed line*. Observation time: **a** 6 August 2008 (0700 LT), **b** 24 August 2009 (1800 LT), **c** 25 August 2009 (0130 LT)

driven) forcing is likely to lead to similar generation processes and structuring of the capping-inversion layer.

3.2.3 A Comparative Study of Three Capping Inversions

Structures of the three exceptional capping inversions identified in Fig. 4 (6 August 2008 at 0700 LT, 24 August 2009 at 1800 LT, 25 August 2009 at 0130 LT) have been analyzed, and their inner structures are presented with normalized dimensions in Fig. 7, with a three-point weighted average smoothing. The upper panels show the three capping inversions as observed, the lower panels present the inner structures of the inversions. Each of the three structures has a primary peak with the maximum value of $(\mathrm{d}T/\mathrm{d}Z)_N$ (marked as I), and secondary peaks with lower values of $(\mathrm{d}T/\mathrm{d}Z)_N$ (II, IIa). The primary peaks have the maximum $(\mathrm{d}T/\mathrm{d}Z)_N$ values (circled) at $0.33Z_N$, $0.49Z_N$ and $0.43Z_N$ of the inversion layers in panels a, b, c, respectively; their structures include a narrow maximum (about 10 % of the total Z) and adjacent "shoulders" (marked with ellipse) with smaller $\mathrm{d}T/\mathrm{d}Z$ values (80–99 %

Table 3 Normalized dimensions of the inner structures in Fig. 7: rows (a), (b) and (c) correspond to the structures in panels (a), (b), and (c), respectively: primary peaks (I) and secondary peaks (II, IIa)

Dimensions (normalized)		(a)	(b)	(c)
Peak I	Symmetry	$0.33Z_N$	$0.49Z_N$	$0.43Z_N$
	Width (circle)	0.13	0.13	0.10
	"Shoulders" width (ellipse)	0.18	0.11	0.18
Peak II	x coordinate	0.18	0.39	0.59
	z coordinate	0.82	0.81	0.79
Peak IIa	x coordinate	0.65	0.59	–
	z coordinate	0.14	0.26	–

of the maximum); due to the "shoulders" pattern these inner structures may be classified as a flat peak type (Sect. 3.2.4). The secondary peaks show a flat shape, where a few adjacent points have similar $\mathrm{d}T/\mathrm{d}Z$ values. Dimensions of the three inner structures are presented in Table 3.

Based on the pattern similarity as demonstrated in Fig. 7 and Table 3 it is suggested that panels (b) and (c) present inner structures of the same inversion layer, showing the primary normalized $\mathrm{d}T/\mathrm{d}Z$ peak at coordinates (0.95; 0.49) and (0.96; 0.43), respectively, although they were observed at different locations and times. The $(\mathrm{d}T/\mathrm{d}Z)_N$ was normalized by dividing each $(\mathrm{d}T/\mathrm{d}Z)$ by $(\mathrm{d}T/\mathrm{d}Z)_{\max}$: viz 1.1, 2.2, 2.6 K $(100\ \mathrm{m})^{-1}$ in (a), (b), (c) respectively, and Z_N was normalized by 126, 189 and 145 m respectively. The similarity of the Aug08 structure in panel (a), to the structures of Aug09 layers in panels (b) and (c), supports the findings in Sect. 3.2.2.

3.2.4 *Categories of the Identified Inversion Inner Structures*

Following the aforementioned findings the study was extended to inversion layers above the capping inversion and up to $z = 3000$ m. A total of 50 inversion layers were analyzed, where 70 % of them had $\Delta H < 150$ m and only 10 % had $\Delta H > 200$ m. Some of the inner structures presented a very strong thermal stratification and well-defined structure (as in Fig. 9), while others showed only a mild pattern. All 50 inner structures were sorted, and five categories of inversion inner structure were defined: symmetric peak, asymmetric peak, double peak, flat peak, and zig-zag. The symmetric peak category was defined by the position of the primary peak, with respect to $\Delta H/2$. Most layers that were classified in the zig-zag category were inversions with very small $\Delta T_{\mathrm{layer}}$. It should be noted that a zig-zag pattern might not represent a real physical property but rather reflect noisy data. An analysis of profiles from different seasons in the Haifa region (unpublished) gave supportive results, where patterns of the defined categories were observed, although there were fewer inversions in each profile.

Examples of the five defined categories are presented in Fig. 8 (in parenthesis, the percentage of cases): symmetric peak (20 %), asymmetric peak (26 %), double peak (12 %), flat peak (28 %), and zig-zag (14 %). To sum up, 46 % of the cases were defined with an evident primary peak (either symmetric or asymmetric), and a total of 86 % of the cases showed a defined pattern.

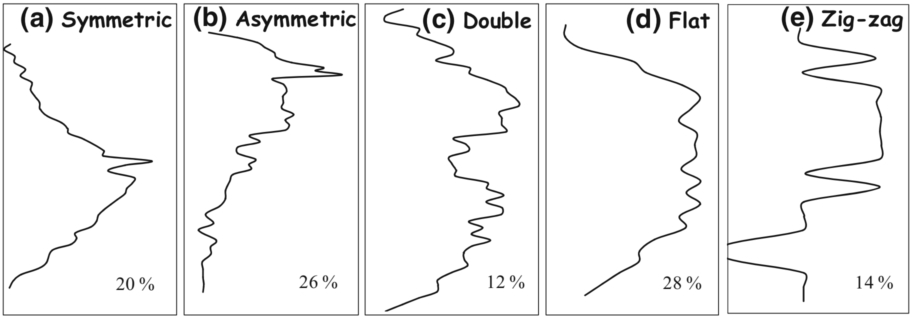

Fig. 8 Examples of the five defined inner structure categories: **a** symmetric peak, **b** asymmetric peak, **c** double peak, **d** flat peak, and **e** zig-zag pattern. Percentage of cases in each category is indicated on the *panels*

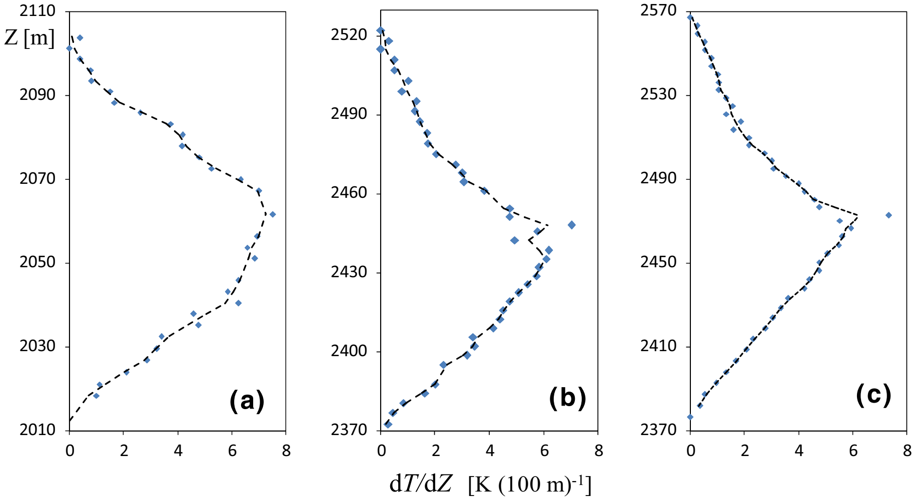

Fig. 9 Symmetric inner structures of consecutive three elevated inversion layers, observed over site *B* on 4 August 2008 at 1900 LT (**a**), over site *A* at 0500 LT the following morning (**b**), and over site *B* at 0600 LT (**c**)

3.3 Analysis of the Evolution of Inversion Layers

Based on the patterns above, consecutive profiles were carefully scanned, in search of similar structures. Several such clear sets were identified, three of which are presented in the following Sects. 3.3.1–3.3.3. The first set is of symmetric inversion layers (Sect. 3.3.1), the second set is of double-peak layers (Sect. 3.3.2), and in Sect. 3.3.3 two consecutive profiles are analyzed employing the structure definitions. The smoothing method as in Sect. 3.2.3.

3.3.1 Case One: Elevated Inversions with Symmetric Inner Structure

A set of three elevated inversions in consecutive "night" profiles was identified, starting close to sunset on 4 August 2008 (Fig. 9, panel a) and ending before sunrise the next morning (panels b, c). The three inner structures were classified as symmetric, with a large vertical temperature gradient. The first inversion in the set (panel a) was observed over Mt. Carmel (site B). It is suggested that this inversion layer was elevated by about 300 m and deepened during the night, showing larger ΔH and larger $\Delta T_{\mathrm{layer}}$ by the following morning over the same site (panel c) and over site A (panel b). The basic dimensions H_{b} and ΔH of the three inversions were: (2020, 85), (2370, 146), (2380, 190) m respectively. In consecutive profiles over site A (not shown) measured 1 h past sunrise, an inversion was observed with H_{b} similar to that in the 0500 profile (b) but twice as thick and with a flat peak pattern. In the afternoon profile over site C, an inversion layer showed a pattern similar to panel (a) but twice as deep and further elevated (2479, 168) m. Note that sites A and B are 7 km away from each other with a 220-m elevation difference. The finding presented here reflects a regional strong steady inversion layer, only weakly (or not at all) influenced by the local complex surface; this description fits with the similar synoptic and mesoscale subsidence inversion.

3.3.2 Case Two: Elevated Inversions with Double Peak and Flat Peak Inner Structure

Naturally, not all structures were as clearly defined as in Fig. 9, and such an example is demonstrated in the following case. Elevated inversions were identified in three consecutive profiles, presenting significant differences in H_{b}, ΔH, and $\Delta T_{\mathrm{layer}}$ as reflected in the upper panel of Fig. 10. The $\Delta T_{\mathrm{layer}}$ values for the inversions in panels a, b, c are 2.6, 1.9, 0.8 K respectively. The 0500 and 0700 LT profiles were observed over site A, the 0600 LT profile over site B (6 August 2008), and the first impression is that these are different layers. However, a close look into the inner structures revealed a possible reflection of an inversion evolution. The inversion showed in panel (c) presented H_{b} similar to that of the upper peak in panel (a); its structure was classified as a flat peak, which resembles the upper peak in panel (b). Careful analysis of the lower peaks shows that while in panel (a) the maximum value of $\mathrm{d}T/\mathrm{d}Z$ is 90 % of the upper peak maximum; in panel (b) it is 66 %, and in profile (c) it is only 15 % (not shown) of the upper peak maximum. The "saddle" between the peaks fell to zero in profile (c). Therefore, the inversion in panel (c) is possibly an evolution of the upper peak of the earlier layer (panels a, b), while the lower part of that inversion practically decayed.

This case study suggests an evolution of a double-peak inversion layer as follows: the layer may break into two separate layers, each with a different further evolution including ascending or descending, and possibly only one of the parts remains along the whole inversion lifetime.

3.3.3 Case Three: Multi-inversion Profiles

In the following case, the inner structure categorization enabled a potentially more precise identification of an inversion layer, and therefore an improved insight into the evolution of the thermal profile. Two of the profiles from the previous section ((a) and (c)) were analyzed up to 1200 m. The 0500 LT profile had three inversion layers and the 0700 LT profile had only two. The challenge was to verify the inversion layers' temporal evolution between the observations, and attempt to identify which of the inversions disappeared. Figure 11 presents the inversion layers as observed in both profiles (marked A–E).

In Fig. 12 the inner structures of all five inversions are presented, where each column corresponds to one profile. The values of ΔH and $\Delta T_{\mathrm{layer}}$ are indicated at the bottom of each frame. An analysis based on H_{b} and ΔH as sole identifiers, might lead to the conclusion that layer B was elevated by 100 m and become layer D, since both layers showed $\Delta H = 113$ m.

However, $\Delta T_{\mathrm{layer}}$ values for inversion layers B and D present a large difference, and when the inner structure methodology is applied, it appears that layer B more likely became layer E since both share a similar inner structure and $\Delta T_{\mathrm{layer}}$ values. This hypothesis, however,

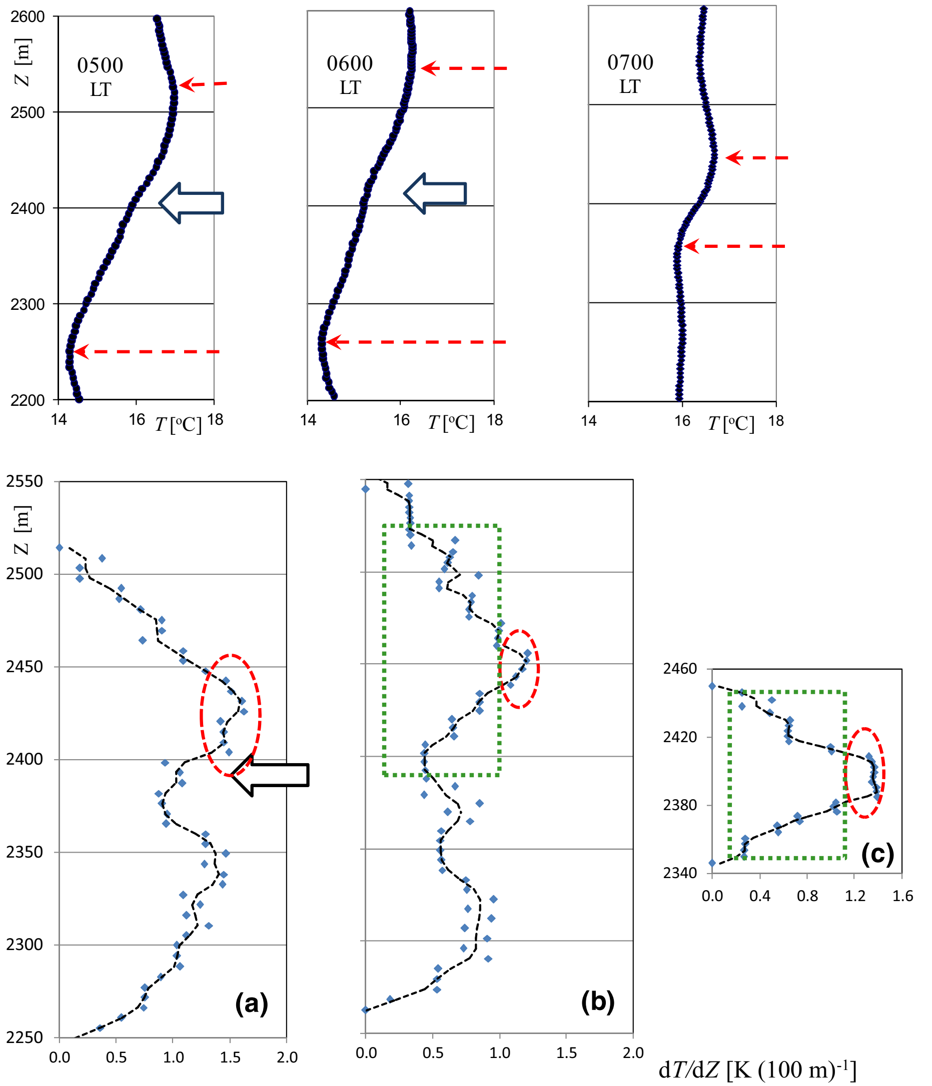

Fig. 10 The inner structures of three elevated inversion layers over site *A* on 6 August 2008 at 0500 LT (**a**), site *B* at 0600 LT (**b**), and site *A* at 0700 LT (**c**). Similar parts of the inner structures are marked with *ellipse* (flat peak) and *rectangle* (local peaks/steps). The structure in panels **a** and **b** is classified as double-peak. The *upper panels* present the temperature profiles as observed where the *arrows* point at the inversions edges (*dashed*) and the "saddle" zone (*white*)

raises a question whether layer B could be elevated by 400 m in only two hours. A possible explanation might be related to the katabatic flow from Mt. Carmel that sometimes tends to persist after sunrise, as was also simulated by the numerical Regional Atmospheric Modeling System (RAMS) model over the campaign period (not shown). Another possibility may relate to downslope flow formed over the morning sunlit heated Mt. Carmel slopes, due to the ridge curvature (Rotach and Zardi 2007). These winds may initiate a vertical circulation before the CBL develops. The profiles in panel (b) present a fast warming from surface up to 300

Fig. 11 Two consecutive morning profiles over site *A*, observed an hour before sunrise (6 August 2008, 0500 LT), and an hour after sunrise (0700 LT). Inversion layers are marked *A*–*E*

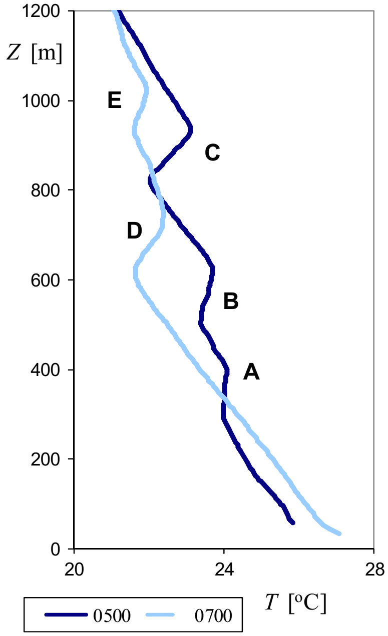

m. The two processes together might initiate significant vertical circulation throughout the early morning hours of 0600–0800 LT.

Although layer A seems very weak and shallow, its altitude below Mt. Carmel summit may have caused this layer to function as a lid to the air pollutants below, as was actually observed on site. Air pollution plumes were observed as capped close to Mt. Carmel top, around 0500 LT. The meaning is that layer A served as the capping inversion. Based on the inner structure methodology, it is concluded that this layer was not observed in the later profile.

4 Summary and Conclusions

Here, the necessity of an explicit identification of inversion layers, as a basic requirement for understanding the spatial and temporal evolution of such layers, is suggested. It was demonstrated that even when the inversion thickness ΔH was measured adequately, it was not sufficient for an accurate definition of a layer.

Hence, the inner structure of inversion layers was explored. The identified patterns can be classified into five categories: symmetric peak, asymmetric peak, double peak, flat peak and zig-zag. It was found that the symmetric peak was associated with the strongest inversions; a set of such elevated inversions presented a relatively long lifetime of the order of 12–24 h and was related to regional subsidence. Strongest triangular structure of the symmetric peak was also found as related to a sharp decrease in relative humidity (not shown). Based on the analysis of consecutive profiles, it is suggested that the "double peak" inversions are likely to break apart into two layers or alternatively one peak remains while the other vanishes. The zig-zag pattern was related to the weakest inversions, and occasionally to noisy data. It was demonstrated that an inversion layer could be explicitly defined by its inner structural

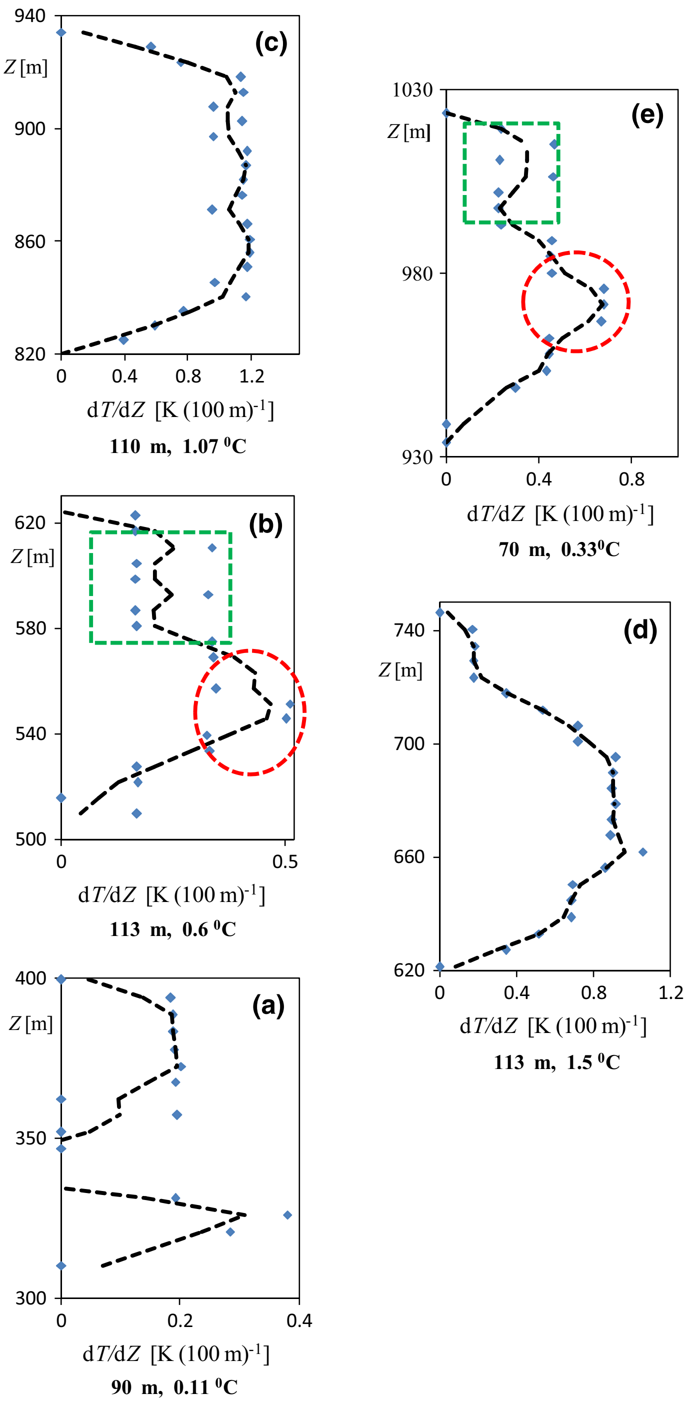

Fig. 12 The inner structures of inversion layers *A*–*E*, presented on $\mathrm{d}T/\mathrm{d}Z$ diagram. The *numbers* at the bottom of each frame indicate ΔH [m] and $\Delta T_{\mathrm{layer}}$ [°C]. Similar structures are marked with *ellipse* and *rectangle* (layers *B* and *E*)

dimensions, in addition to the basic dimensions proposed in the literature i.e., H_b and ΔH. This application was used to track inversion layer and to investigate its structural evolution and variations of its dimensions. For capping-inversion layers, the relation which was found between H_b and ΔH suggests that, in many cases, the lower layers (small H_b) tend to be deeper (larger ΔH).

It is suggested that the inner structure of an inversion layer has a finite lifetime, and therefore it may be used to track the spatial and temporal evolution of inversions. Regional factors such as topography and gravity waves may play an important role in the thermodynamics of the inner structures. However, at this time, we have no integrated explanation for the lifetime or pattern mechanism.

Acknowledgments The authors would like to thank those who contributed to this study by sharing facilities, data, time, goodwill and advice: Haifa Towns Association for the Environment Protection, Israel Electric Corporation (in Haifa and Tel-Aviv), Kishon River Authority (Haifa), Ministry of the Environment Protection (Air Monitoring division, Tel-Aviv), Sea-Gal Yacht Club (Hertzlia), and special thanks to Jakob Kutsher for his help. We thank Roland Stull for his very helpful comments on the draft, and the anonymous reviewers for their important remarks. This work was supported by the IAEC-Pazi Foundation.

References

Alpert P, Abramsky R, Neeman BU (1990) The prevailing summer synoptic system in Israel—subtropical high, not Persian Trough. Israel J Earth Sci 39:93–102

Berner AH, Bretherton R, Wood CS (2011) Large-eddy simulation of mesoscale dynamics and entrainment around a pocket of open cells observed in VOCALS-Rex RF06. Atmos Chem Phys 11:10525–10540

Brooks IM (2003) Finding boundary layer top: application of a wavelet covariance transform to lidar backscatter profiles. J Atmos Ocean Technol 20:1092–1105

Dayan U, Koch J (1988) Analysis of upper-air measurements in Haifa Region, for indication of the critical conditions for tall plumes transport and dispersion. Report for the Israel Environmental Protection Service, Hebrew

Deardorff JW (1979) Prediction of convective mixed-layer entrainment for realistic capping inversion structure. J Atmos Sci 36:424–436

Deardorff JW, Willis GE, Stockton BH (1980) Laboratory studies of the entrainment of a convectively mixed layer. J Fluid Mech 100:41–64

Fedorovich EE, Mironov DV (1995) A model for shear-free convective boundary layer with parameterized capping inversion structure. J Atmos Sci 52:83–95

Gossard EE, Gaynor JE, Zamora RJ, Neff WD (1985) Fine structure of elevated stable layers observed by sounder and in situ tower sensors. J Atmos Sci 42(20):2156–2169

Grabon JS, Davis KJ, Kiemle C, Ehret G (2010) Airborne lidar observations of the transition zone between the convective boundary layer and free atmosphere during the International H_2O Project (IHOP) in 2002. Boundary-Layer Meteorol 134:61–83

Gryning SE, Batchvarova E (1994) Parameterization of the depth of the entrainment zone above the daytime mixed layer. Q J R Meteorol Soc 120:47–58

Jones CR, Bretherton CS, Leon D (2011) Coupled vs. decoupled boundary layers in VOCALS-Rex. Atmos Chem Phys 11:7143–7153

Kallos G, Astitha M, Katsafados P, Spyrou C (2007) Long-range transport of anthropogenically and naturally produced particulate matter in the Mediterranean and North Atlantic: current state of knowledge. J Appl Meteorol Climatol 46:1230–1251

Koch J, Dayan U (1992) A synoptic analysis of the meteorological conditions affecting dispersion of pollutants emitted from tall stacks in the coastal plain of Israel. Atmos Environ 26:2537–2543

Mahrt L (1979) Penetrative convection at the top of a growing boundary layer. Q J R Meteorol Soc 105:969–985

Martucci G, Matthey R, Mitev V, Richner H (2007) Comparison between backscatter lidar and radiosonde measurements of the diurnal and nocturnal stratification in the lower troposphere. J Atmos Ocean Technol 24(7):1231–1244

Melas D, Ziomas IC, Zerefos CS (1995) Boundary layer dynamics in an urban coastal environment under sea-breeze conditions. Atmos Environ 29(24):3605–3617

Metcalf JI (1975) Gravity waves in a low-level inversion. J Atmos Sci 32:351–361

Piringer M, Baumann K, Langer M (1998) Summertime mixing heights at Vienna, Austria, estimated from vertical sounding and by a numerical model. Boundary-Layer Meteorol 89:25–45

Rampanelli G, Zardi D (2004) A method to determine the capping inversion of the convective boundary layer. J Appl Meteorol 43:925–933

Rotach MW, Zardi D (2007) On the boundary-layer structure over highly complex terrain: key findings from MAP. Q J R Meteorol Soc 133:937–948

Saiki EM, Moeng CH, Sullivan PP (2000) Large-eddy simulations of the stably stratified planetary boundary layer. Boundary-Layer Meteorol 95:1–30

Seibert P, Beyrich F, Gryning SE, Joffre S, Rasmussen A, Tercier P (2000) Review and intercomparison of operational methods for the determination of the mixing height. Atmos Environ 34:1001–1027

Stull R (1988) An introduction to boundary layer meteorology. Kluwer Academic Press, Dordrecht 666 pp

Stull RB (1991) Static stability—an update. Bull Am Meteorol Soc 72:1521–1529

Sullivan PP, Moeng CH, Srevens B, Lenschow DH, Mayor SH (1998) Structure of the entrainment zone capping the convective atmospheric boundary layer. J Atmos Sci 55:3042–3064

Sun JN (2009) On the parameterization of convective entrainment: inherent relationships among entrainment parameters in bulk models. Adv Atmos Sci 26(5):1005–1014

Tennekes H (1973) A model for the dynamics of the inversion above a convective boundary layer. J Atmos Sci 30:558–567

Uzan L, Alpert P (2012) The coastal boundary layer and air pollution—a high temporal resolution analysis in the east Mediterranean coast. Open Atmosph Sci J (TOASJ) 6:9–18

Zeman O, Tennekes H (1977) Parameterization of the turbulent energy budget at the top of the daytime atmospheric boundary layer. J Atmos Sci 34:111–123